Crystal structure of murine 4-1BB and its interaction with 4-1BBL support a role for galectin-9 in 4-1BB signaling

Received for publication, August 29, 2017, and in revised form, December 1, 2017 Published, Papers in Press, December 14, 2017 DOI 10.1074/jbc.M117.814905

Aruna Bitra[‡], Tzanko Doukov[§], Jing Wang[‡], Gaelle Picarda[‡], Chris A. Benedict[‡], Michael Croft[‡‖], and Dirk M. Zajonc[‡]**

*From the [‡]Division of Immune Regulation, La Jolla Institute for Allergy and Immunology (LJI), La Jolla, California 92037, the [§]Stanford Synchrotron Radiation Light Source, Menlo Park, California 94025, the [‖]Department of Medicine, University of California San Diego, La Jolla, California 92037, and the **Department of Internal Medicine, Faculty of Medicine and Health Sciences, Ghent University, 9000 Ghent, Belgium*

Edited by Peter Creswell

4-1BB (CD137) is a TNF receptor superfamily (TNFRSF) member that is thought to undergo receptor trimerization upon binding to its trimeric TNF superfamily ligand (4-1BBL) to stimulate immune responses. 4-1BB also can bind to the tandem repeat–type lectin galectin-9 (Gal-9), and signaling through mouse (m)4-1BB is reduced in galectin-9 (Gal-9)–deficient mice, suggesting a pivotal role of Gal-9 in m4-1BB activation. Here, using sulfur-SAD phasing, we determined the crystal structure of m4-1BB to 2.2-Å resolution. We found that similar to other TNFRSFs, m4-1BB has four cysteine-rich domains (CRDs). However, the organization of CRD1 and the orientation of CRD3 and CRD4 with respect to CRD2 in the m4-1BB structure distinctly differed from those of other TNFRSFs. Moreover, we mapped two Asn residues within CRD4 that are *N*-linked glycosylated and mediate m4-1BB binding to Gal-9. Kinetics studies of m4-1BB disclosed a very tight nanomolar binding affinity to m4-1BBL with an unexpectedly strong avidity effect. Both N- and C-terminal domains of Gal-9 bound m4-1BB, but with lower affinity compared with m4-1BBL. Although the TNF homology domain (THD) of human (h)4-1BBL forms non-covalent trimers, we found that m4-1BBL formed a covalent dimer via 2 cysteines absent in h4-1BBL. As multimerization and clustering is a prerequisite for TNFR intracellular signaling, and as m4-1BBL can only recruit two m4-1BB monomers, we hypothesize that m4-1BBL and Gal-9 act together to aid aggregation of m4-1BB monomers to efficiently initiate m4-1BB signaling.

Tumor necrosis factor molecules are a large superfamily that contains both TNF ligands (TNFSF)[2] and their cognate receptors (TNFRSF) (1–3). Members of this family exert their function by forming aggregated ligand–receptor complexes thereby regulating various immune responses, including multiple aspects of adaptive and innate immunity, as well as lymphoid tissue organization. TNF members can either induce apoptosis by activating caspases (*e.g.* Fas, TNFR1, and TRAILR1) or promote cellular proliferation, survival, and function by activating serine/threonine kinase-dependent pathways (*e.g.* TNFR2, 4-1BB, OX40, and RANK) (1). The specificity of TNF–TNFR interactions and their extracellular activities make them highly attractive targets for therapeutic interventions. To date, a total of 19 TNF ligands and 29 TNF receptors have been reported (2–6) and a number of high-resolution structures of cognate ligand–receptor complexes have allowed an understanding of the molecular architecture important for their specific functions (7–9). The ligands of the TNF family are type II transmembrane proteins containing a canonical TNF homology domain (classic β-sandwich jelly-fold) and generally exist either as membrane anchored or soluble homotrimers (4). TNFRSF molecules are mostly monomeric and highly modular type I transmembrane proteins containing pseudo repeats of extracellular cysteine-rich domains (CRDs).

4-1BB (CD137/TNFRSF9) is a TNFR family member that acts as an inducible costimulatory receptor on activated T cells, as well as NK cells and some dendritic cells (2, 5, 10). It contains four CRDs (11), with CRD1–3 being sufficient for binding to its ligand 4-1BBL (TNFSF9) (12). Human 4-1BBL has a TNF homology domain (THD) similar to other TNF ligands but it forms a unique three-bladed propeller-like homotrimer, unlike the more common canonical bell-shape structures (13, 14). 4-1BBL is induced upon stimulation on various antigen-presenting cells including B cells, macrophages, and dendritic cells (2, 10, 13, 15). Similar to other TNF members, association with 4-1BBL oligomerizes 4-1BB, thereby recruiting intracellular trimeric TRAFs (TRAF1 and TRAF2) leading to activation of NF-κB and phosphatidylinositol 3-kinase/Akt-mediated proin-

This work was supported by NIAID, National Institutes of Health Grant AI110929 (to M. C. and D. M. Z.). The authors declare that they have no conflicts of interest with the contents of this article. The content is solely the responsibility of the authors and does not necessarily represent the official views of the National Institutes of Health.

This article contains Figs. S1–S3.

The atomic coordinates and structure factors (codes 5WJF, 5WI8, and 5WIW) have been deposited in the Protein Data Bank (http://wwpdb.org/).

[1] To whom correspondence should be addressed: Division of Immune Regulation La Jolla Institute for Allergy and Immunology, 9420 Athena Cir., La Jolla, CA 92037. Tel.: 858-752-6605; Fax: 858-752-6985; E-mail: dzajonc@lji.org.

[2] The abbreviations used are: TNFSF, tumor necrosis factor superfamily; TNFRSF, tumor necrosis factor receptor superfamily; 4-1BBL, 4-1BB ligand, Gal-9, galectin-9; CRD, cysteine-rich domain; THD, TNF homology domain; NTD, N-terminal domain; CTD, C-terminal domain; SEC, size exclusion chromatography; r.m.s., root mean square; RANKL, receptor activator of nuclear factor κB; OPG, osteoprotegerin; PNGase F, peptide *N*-glycosidase F; ESI, electrospray ionization; SPR, surface plasmon resonance; GST, glutathione *S*-transferase; RCM, reductive carboxymethylation; PNGase N, peptide:*N*-glycosidase; Bicine, *N*,*N*-bis(2-hydroxyethyl)glycine; CC, correlation coefficient.

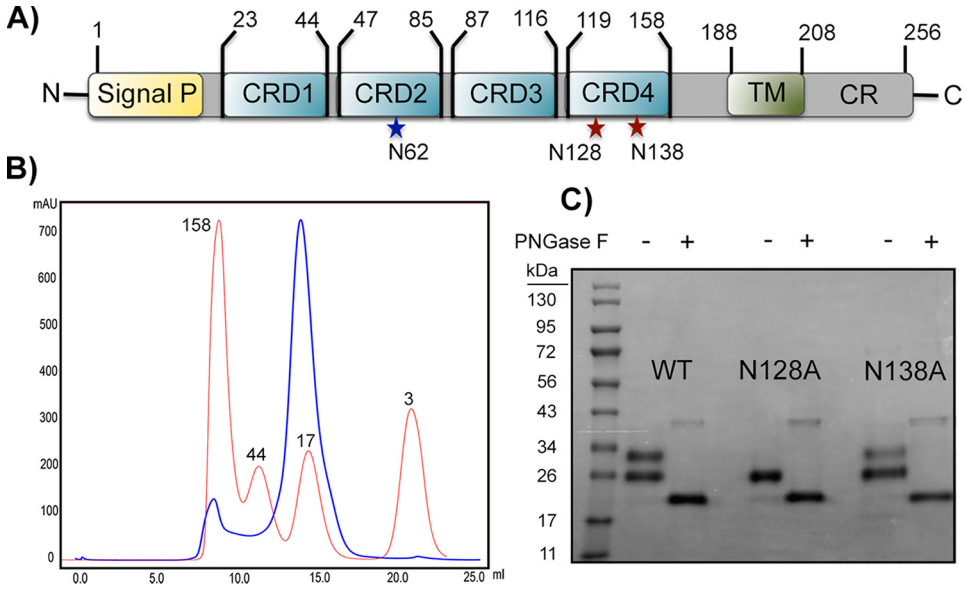

Figure 1. Expression of m4-1BB constructs. *A,* domain organization of m4-1BB. *Signal P*, signal peptide; *pCRD1*, partial CRD1; *TM*, transmembrane region; *CR*, cytoplasmic region containing TRAF binding motif. *, potential *N*-linked glycosylation sites indicated. *B,* size exclusion chromatogram of wildtype (*WT*) m4-1BB (*blue line*) and molecular weight marker as a reference (*red line*). *C,* Coomassie-stained 4–20% SDS-PAGE analysis of purified proteins of m4-1BB (WT), m4-1BB N128A mutant, and m4-1BB N138A mutant with (−*PNGase*) or without (+*PNGase*) *N*-linked glycans. Molecular weights of protein standards are indicated.

flammatory signaling pathways (10, 16–19). Ligation of 4-1BB expressed on T cells with 4-1BBL or agonist antibodies can generate strong costimulatory signals in T cells to promote their clonal expansion and activation state (20), relevant for tumor immunity and boosting immunity against viruses (6, 10, 16, 21).

As well as binding 4-1BBL, we recently identified a novel carbohydrate-mediated interaction between 4-1BB and galectin-9 (Gal-9), a member of an unrelated animal lectin family, and demonstrated in several immune responses that Gal-9 played a significant role in 4-1BB signaling activities (12). Gal-9 is a bivalent tandem repeat–type lectin possessing both N-terminal (NTD) and C-terminal (CTD) carbohydrate-binding domains (22, 23) that recognize specific oligosaccharide side chains on cell surface receptor proteins (24, 25). Gal-9 binds to terminal galactose moieties of *N*-linked glycans within the CRD4 region of 4-1BB. The binding of Gal-9 to 4-1BB does not compete with the binding of 4-1BB to its natural ligand 4-1BBL or to agonist antibodies against 4-1BB. We demonstrated that Gal-9 facilitates signaling and functional activation of 4-1BB in mouse T cells, dendritic cells, and natural killer cells upon binding mouse 4-1BBL or agonist antibodies to 4-1BB. We hypothesized that Gal-9 acts as an essential bridge to allow the spatial orientation of individual 4-1BB monomers thereby enabling the clustering of 4-1BB– 4-1BBL or 4-1BB–antibody oligomeric complexes to allow stable recruitment of cytoplasmic signaling components. Here, to delineate the molecular and mechanistic principles underlying the assembly of these protein complexes, we have characterized the interaction between m4-1BBL and m4-1BB. Furthermore, we studied the interaction of m4-1BB with both N- and C-terminal domains of Gal-9 and determined the crystal structure of the m4-1BB receptor. Together, our studies shed light on the role of Gal-9 in clustering m4-1BB for optimal signaling.

Results

Generation of m4-1BB

Mouse 4-1BB has four CRDs (residues 23–160) followed by a single transmembrane region (residues 188–208) and a cytoplasmic domain (residues 209–256) that is necessary for the binding of adaptor proteins to facilitate signaling (Fig. 1*A*). Two *N*-linked glycosylation sites (N-*X*-S/T) are located within CRD4 of m4-1BB at residues Asn-128 and Asn-138 (numbering from initiating methionine). In addition, a "cryptic" *N*-linked glycosylation site (N-*X*-C) is located in CRD2 at residue Asn-62 (Fig. 1*A*). We expressed the full-length ectodomain of m4-1BB (residues 24–160) as a thrombin cleavable Fc fusion protein in mammalian HEK293T cells. After affinity purification, the Fc tag was removed by thrombin digestion and the resulting m4-1BB CRD1–4 protein was purified by size exclusion chromatography (SEC, Fig. 1*B*). Fractions containing monomeric m4-1BB were analyzed using SDS-PAGE. Purified wildtype (wt) m4-1BB migrated as two bands of equal intensity. Deglycosylation of wt m4-1BB resulted in a single band of lower molecular weight, suggesting that both bands of the native wt m4-1BB were the result of differential glycosylation (Fig. 1*C*). The upper band most likely represents wt m4-1BB molecules that carry *N*-linked glycans at both Asn-128 and Asn-138, whereas the lower band corresponds to m4-1BB carrying only one *N*-linked glycan at either one of the two asparagines (Asn-128 or Asn-138). Furthermore, to reduce the heterogeneity in glycosylation of m4-1BB, we destroyed both of these glycosylation sites separately using site-directed mutagenesis. Although m4-1BB N128A migrated as a single band on SDS-PAGE that further could be reduced in M_r upon deglycosylation, migration of m4-1BB N138A resembled that of wt m4-1BB with the upper band being slightly less intense (Fig. 1*C*). The appearance of the second upper band for m4-1BB N138A was likely due to a sec-

Table 1
Data collection and refinement statistics

Data collection statistics	4-1BB WT	4-1BBWT	4-1BB N128A
PDB ID	5WJF	5WI8	5WIW
Space group	$P2_12_12$	$P\ 2_1$	$P4_3$
Cell dimension			
a, *b*, *c*, (Å)	65.05, 67.76, 87.99	65.01, 61.76, 110.75	66.63, 66.63, 82.18
α, β, γ (°)	90.00, 90.00, 90.00	90.00, 91.53, 90.00	90.00, 90.00, 90.00
Resolution range (Å) (outer shell)	36.9 – 2.50 (2.60–2.50)	40.0 – 2.95 (3.06 – 2.95)	50.0 – 2.28 (2.32 – 2.28)
No. of unique reflections	14,009 (1,542)	17,070 (1,237)	16,323 (782)
R_{meas} (%)	22.6 (393.3)	15.4 (34.8)	6.5 (39.2)
R_{pim} (%)	1.9 (51.4)	8.4 (19.9)	2.7 (17.1)
Multiplicity	123.3 (107.3)	3.1 (2.4)	5.5 (4.8)
Average $I/\sigma I$	37.5 (3.5)	11.6 (1.92)	22.7 (2.44)
Completeness (%)	99.8 (98.5)	91.8 (67.5)	99.6 (96.0)
Refinement statistics			
No. atoms	2,117	4,333	1,816
Protein	1,999	3,923	1,598
Ligand	40	234	74
Water	78	91	117
Ramachandran plot (%)			
Favored	98.5	96.8	97.6
Allowed	1.5	3.2	1.4
Outliers	0	0	1
R.m.s. deviations			
Bonds (Å)	0.007	0.009	0.006
Angles (°)	1.19	1.49	1.13
B-factors (Å^2)			
Protein	57.6	73.0	45.2
Ligand	97.2	95.5	61.6
Water	56.5	54.8	46.1
Glycerol/EDO/sulfate	None/72.0/none	88.2/72.6/none	83.7/none/42.1
R factor (%)	22.2	23.5	19.6
R_{free} (%)	28.9	27.9	22.7

ondary *N*-linked glycosylation event occurring at the cryptic Asn-62 site in CRD2, because deglycosylation resulted again in the formation of a single band of lower molecular weight (Fig. 1*C*).

Structure determination and overall architecture of 4-1BB

We used both wt m4-1BB as well as m4-1BB N128A mutant for crystallization studies. Although we originally set out to determine the crystal structure of the m4-1BB–Gal-9 (NTD or CTD) complex, we were only able to obtain crystals of m4-1BB (Fig. S1). Crystals were obtained in two different space groups; $P2_1$ with 4 molecules in the asymmetric unit and $P2_12_12$ with two molecules in the asymmetric unit (Fig. S2, *A* and *B* and Table 1). Similarly, when using the m4-1BB N128A construct, we obtained only m4-1BB crystals in space group $P4_3$ with two molecules in the asymmetric unit (Fig. S2*C* and Table 1). Experimental phasing using sulfur-SAD was used to determine the structure of the m4-1BB in space group $P2_12_12$ to a final resolution of 2.5 Å, whereas structures of the other two space groups were subsequently determined using Molecular Replacement.

The ectodomain of m4-1BB folds into an elongated molecule composed of four CRDs (Fig. 2*A*). All 20 cysteine residues participate in intradomain disulfide bridges that maintain the stability and the integrity of the entire ectodomain. Although CRD1 and CRD4 contain 2 disulfide bridges each, CRD2 and CRD3 each contain 3 disulfide bridges. CRD3 and CRD4 are rotated by 30 degrees perpendicular to the rotation axis leading to a slight bend in the central part of the molecule (Fig. 2*A*).

The crystal structure of the m4-1BB ectodomain also revealed the location of the two *N*-linked glycosylation sites at positions Asn-128 and Asn-138. Both *N*-linked glycans are exposed, present at the bottom of the CRD4, and are opposite to each other. The crystal structure of HEK293T expressing m4-1BB illustrated that Asn-138 is always glycosylated, whereas Asn-128 shows only partial glycosylation. In the $P2_1$ space group, all of the four 4-1BB monomers exhibited *N*-linked glycosylation at Asn-138, whereas only one monomer contained electron density for a single *N*-acetylglucosamine at Asn-128 (Fig. 2*B*). Similarly, in the $P2_12_12$ crystal of 4-1BB the *N*-linked glycan is missing at Asn-128. However, electron density at the Asn-138-linked *N*-acetylglucosamine residue was observed. The extent of electron density for individual glycans differed but in the cases where no *N*-linked glycan was present, no electron density was connected to Asn-128. This dissimilarity in the glycosylation pattern at both of these positions suggests an explanation for the existence of two crystal forms of m4-1BB. The SSM superposition of 4-1BB monomers of all these space groups superposed well with a root mean square deviation (r.m.s. deviation) of 0.8 Å indicating a stable overall-fold. However, all of these monomers of m4-1BB differed in the orientation of *N*-linked glycans at both Asn-128 and Asn-138 and there existed some rotational freedom between individual *N*-linked glycans (Fig. 2, *B* and *C*). The individual glycans project away from m4-1BB to allow Gal-9 binding.

The interfaces between 4-1BB molecules in three crystal forms are stabilized by various hydrogen bonding and hydrophobic interactions between the head-to-tail-oriented 4-1BB monomers. This antiparallel orientation occurred in all three space groups. Due to this arrangement, the CRD1 region of each molecule becomes stabilized by the *N*-linked glycan at positions Asn-128 and Asn-138 of the opposing molecule (Fig. S2). From the crystal structure it was obvious that the *N*-linked

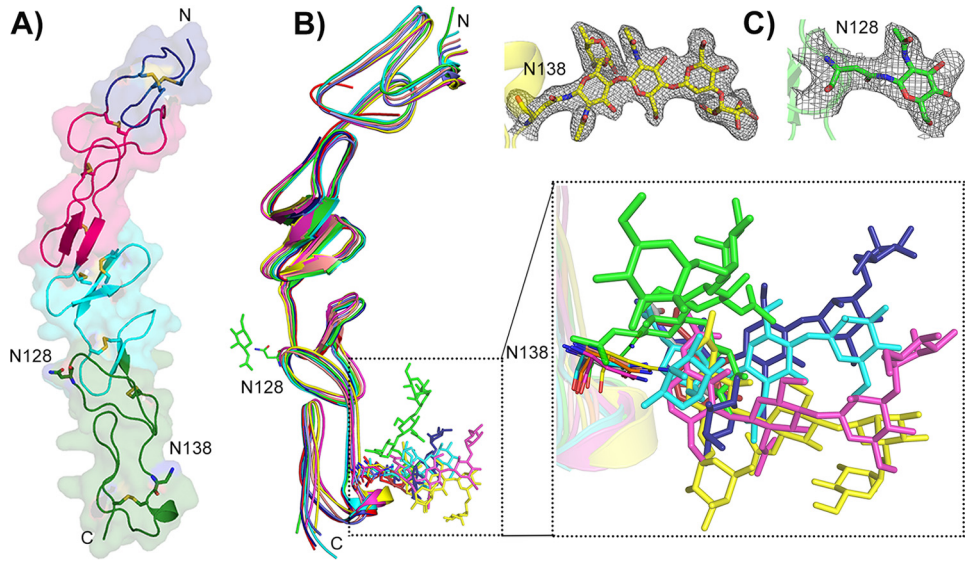

Figure 2. Structure of m4-1BB. *A,* ribbon representation of m4-1BB with transparent molecular surface colored differently for each cysteine-rich domain. *CRD1,* blue; *CRD2, magenta*; CRD3, *cyan*; CRD4, *green*. All cysteine residues and Asn residues that undergo *N*-linked glycosylation are shown as *sticks*. *B,* superposition of all monomers of 4-1BB from the three different space groups $P2_1$, $P2_12_12$, and $P4_3$, showing the well ordered overall structure as well as the variation in the relative spatial orientation of *N*-glycans at Asn-138 position. *C,* representative $2F_o - F_c$ electron density map contoured at 1σ, for *N*-glycans at positions 128 and 138 within the CRD4 region. All *N*-linked glycans at Asn-128 and Asn-138 are shown as *sticks*. All figures were made in PyMOL.

glycan at both positions helped in the proper anchoring of CRD1 either within the same 4-1BB molecule or the adjacent molecule. Based on our crystal structures, we propose that the absence of this sugar anchorage disturbs the arrangement of CRD1 as evident from the lack of proper electron density for the CRD1 region in the crystal structure of m4-1BB N128A mutant, suggesting this region is disordered (Fig. S2*C*).

Although the sequence identity among TNFRSF members is less than 30%, they maintain a remarkable structural preservation. They all share a common structural-fold that differs in the number of individual CRDs, as well as the overall curvature of the elongated receptor (7, 8, 26–28). The CRDs of m4-1BB contain both A and B type modules, which are typical for members of the TNFR superfamily (29). Both modules are further differentiated based on their amino acid composition and disulfide connectivity. Because CRD1 of 4-1BB contains only one B2 type module as it lacks the conserved antiparallel β-strand motif, it is only a partial CRD. The CRD2 of 4-1BB contains one A1 module with one disulfide bond and a long C-shaped loop, as well as one B2 motif made up of antiparallel β-strands with 1–3 and 2–4 (order of consecutive cysteines within the CRD) disulfide connectivity and an S-shaped type-fold (Fig. 3*A*). Both A1 and B2 modules are stabilized by various hydrogen bonding and hydrophobic interactions among the corresponding residues. The CRD3 of m4-1BB contains both A1 and A2 modules similar to that observed in TNFR2 (8). The A2 module has the consensus sequence of the A1 module with an additional disulfide linkage within the domain, as a result CRD3 of m4-1BB exhibits 1–4 and 2–3 disulfide linkages (Fig. 3*B*). Analogous to TNFR2, due to the presence of this extra 2–3 disulfide linkage between Cys-93 and Cys-98, the β turn motif that connects strands 2 and 3 gets deflected (Fig. 3*C*) and also the space that is present between CRD2 and CRD3 regions in the case of other TNFR members becomes buried in 4-1BB. In contrast, CRD4 of 4-1BB differs from the remaining three CRDs, as it has A1 and

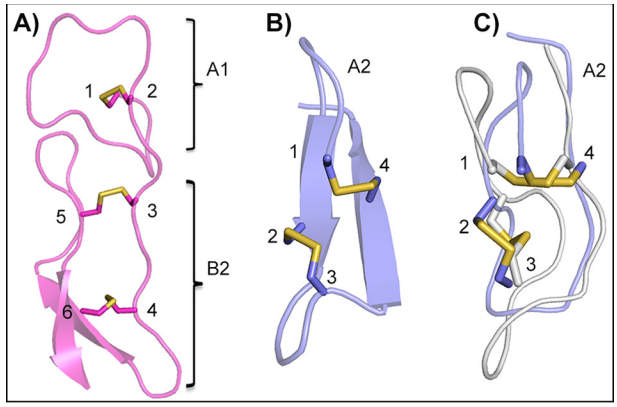

Figure 3. Organization of type A and B modules. *A,* close up view of CRD2 of m4-1BB showing A1 and B2 modules with their disulfide connectivity. *B,* schematic representation of A2 module present in CRD3 of m4-1BB. *C,* structural alignment of A2 subdomain of m4-1BB and TNFR2 (PDB code 3ALQ). m4-1BB is shown in *blue* and TNFR2 is *gray*. In all panels, the sulfur atoms of disulfide linkages are shown as *yellow sticks*. All figures were made in PyMOL.

B1 modules rather than A1 and B2 types. The B1 module has a similar amino acid sequence and the spacing of cysteine residues according to the B2 module, however, in CRD4, the 3–5 disulfide linkage is missing and the corresponding cysteines are replaced by aromatic/smaller amino acids like tryptophan and glycine.

Comparison with structures of other TNF receptors

4-1BB shares low sequence identity with other known TNF receptors. For example, 4-1BB has ~30% sequence identity with TNFR1 (TNFRSF1A), RANK (TNFRSF11A), HVEM (TNFRSF14), LTβR (TNFRSF3), and CD40 (TNFRSF5). To identify the TNF receptors that are most structurally related to 4-1BB, we performed a DALI search using 4-1BB. The top DALI hits were RANK, CD40, HVEM, TRAILR2/DR5, DcR3, TNFR2, and DR6 with Z scores ranging from 9.3 to 8.2 with around 100–120 residues of each corresponding TNFR mem-

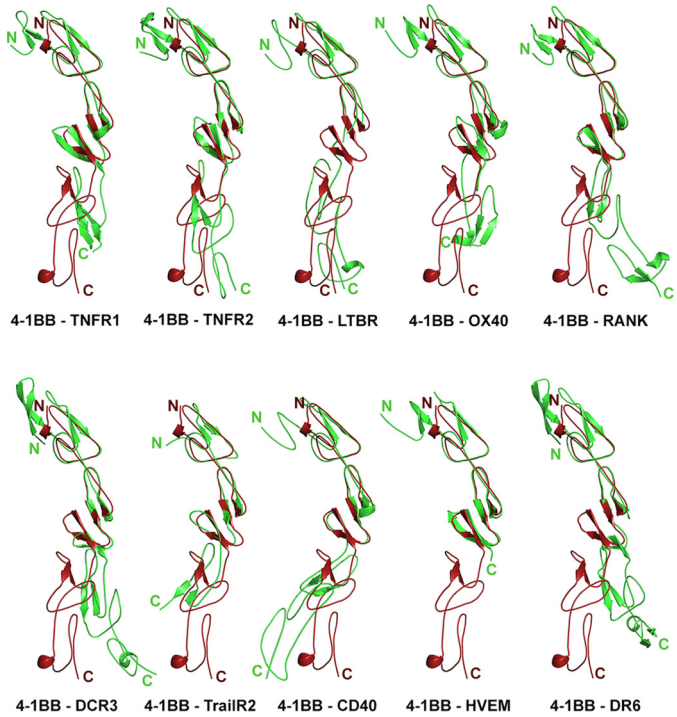

Figure 4. Superimposition of m4-1BB with other TNFRSF members. Structural alignment of m4-1BB (*red color*) with various TNFRSF members (*green color*) based on the Cα atoms of CRD2 region reveals structural differences at CRD1, CRD3, and CRD4 regions. PDB codes of crystal structures of TNFR members used for superposition are as follows: TNFR1, 1TNR; TNFR2, 3ALQ; LTbR, 4MXW; OX40, 2HEV; RANK, 3ME4; DcR3, 3MHD; TRAILR2, 4I9X; CD40, 5DMJ; HVEM, 4FHQ; DR6, 3QO4). All figures were made in PyMOL.

ber aligned with 4-1BB. Even though there is about 30% sequence identity with TNFR1, the DALI did not show TNFR1 as a strongly structurally related molecule. Superposition of 4-1BB with the top DALI hits as well as other molecules that were not as highly scored (OX40, LTβR) resulted in large root mean square deviations of greater than 5 Å between the Cα atoms (Fig. 4). The major difference between 4-1BB and other TNFRs lies in the structural organization and relative orientation of CRD1, CRD3, and CRD4. CRD1 of 4-1BB is only a partial CRD with only 2 disulfide bridges and lacks one of the canonical disulfide linkages seen in other TNFRs that in general contain 3 disulfide bridges (Fig. S3). As a result, CRD1 of 4-1BB is much smaller than the corresponding CRD1 of other TNFR members. Additionally, β1- and β2-strands that are present in CRD1 of all TNF receptors are replaced by a long loop, hence making the architecture of CRD1 unique compared with other TNFR members (Fig. S3*B*). In contrast, CRD2 of 4-1BB shares similar structural features and superimposed well with r.m.s. deviation values less than 1 Å with known TNFRs despite the lack of appreciable levels of sequence identity (Fig. S3*C*). On the other hand, bending in the central hinge region of m4-1BB that joins CRD2 and CRD3 changes the orientation of CRD3 and CRD4 distinctly with respect to corresponding regions of other TNFR members and hence they cannot be superposed on any other receptor. In most of the TNF–TNFR complexes this central hinge region forms specific binding interactions, for example, in the case of the RANKL–OPG complex, due to a central twist, the CRDs of OPG can reach the binding interface to occupy two RANKL molecules simultaneously (27). In general, TNFR members use CRD1, CRD2, and CRD3 (*e.g.* OX40) or only CRD2 and CRD3 (*e.g.* RANK, TNFR1) as the binding interface to interact with their TNF ligands (30). In the case of m4-1BB, prior studies have suggested that CRD 1–2 contribute to ligand binding (12, 31). Because CRD3 and -4 are rotated, compared with CRD3 and -4 of other TNFRSF members (Fig. S3), it is possible that upon m4-1BBL binding the geometry of the m4-1BB–m4-1BBL complex will be sufficiently distinct to other complexes that only a suboptimal association with intracellular TRAFs can occur. This correlates to the requirement for Gal-9 for efficient signaling through m4-1BB as Gal-9 induces clustering of the 4-1BB monomers, thus facilitating association with TRAFs.

Dimerization of m4-1BB ligand ectodomain

The affinities of TNF–TNFR interactions mainly depends on the oligomeric state of the complex (32). To get a deeper insight into the multimeric association of m4-1BB with m4-1BBL, we expressed m4-1BBL and studied the affinity of interaction with its receptor. Mouse 4-1BBL is a 33-kDa type II transmembrane protein composed of an N-terminal cytoplasmic domain (amino acids 1–80), a transmembrane region (amino acids 83–103), and a C-terminal extracellular region encompassing the THD (amino acids 147–300) (Fig. 5*A*). The THD of m4-1BBL shares around 40% sequence identity with its human homologue and ~25% identity with other TNF family ligands. We expressed the THD of m4-1BBL (residues 139–309) in *Sf*9 insect cells and removed the hexahistidine and birA tag by thrombin digestion. On a standardized SEC column (Superdex S200, 16/60 GE Healthcare), m4-1BBL eluted as a monodisperse peak between the 44- and 17-kDa reference peaks, whereas each m4-1BBL subunit has a calculated molecular mass of 19.3 kDa excluding *N*-linked glycans (Fig. 5*B*). When we subjected the SEC peak fractions to SDS-PAGE, purified m4-1BBL migrated under non-reducing conditions as a sharp band close to the 56-kDa molecular mass marker (Fig. 5*C*). Under reducing conditions, m4-1BBL migrated at roughly half that size, indicating that the m4-1BBL THD forms disulfide-linked dimers, rather than trimers as observed for human (h)4-1BBL. The PNGase F-treated m4-1BBL migrated as expected close to its calculated molecular mass of 19.3 kDa under reducing conditions, suggesting that the *N*-linked glycans reduce overall mobility of m4-1BBL during SDS-PAGE. To confirm its disulfide-linked homodimeric state, m4-1BBL was fully reduced to a monomer using reductive *S*-carboxymethylation and analyzed using mass spectrometry, in comparison to native, unmodified m4-1BBL. As expected, the cysteines in m4-1BBL were reduced and blocked by carboxymethylation and the protein migrated as a monomer on SDS-PAGE under both non-reducing and reducing conditions (Fig. 5*C*). In addition, electrospray ionization (ESI)-TOF analysis of both native m4-1BBL and *S*-carboxymethylated protein confirmed its native state to be a dimer (21.9 *versus* 43.8 kDa, Fig. 5, *D* and *E*). A second minor m4-1BBL species was also found with molecular masses of ~23.0 and ~44.9 kDa. This species is likely two times glycosylated

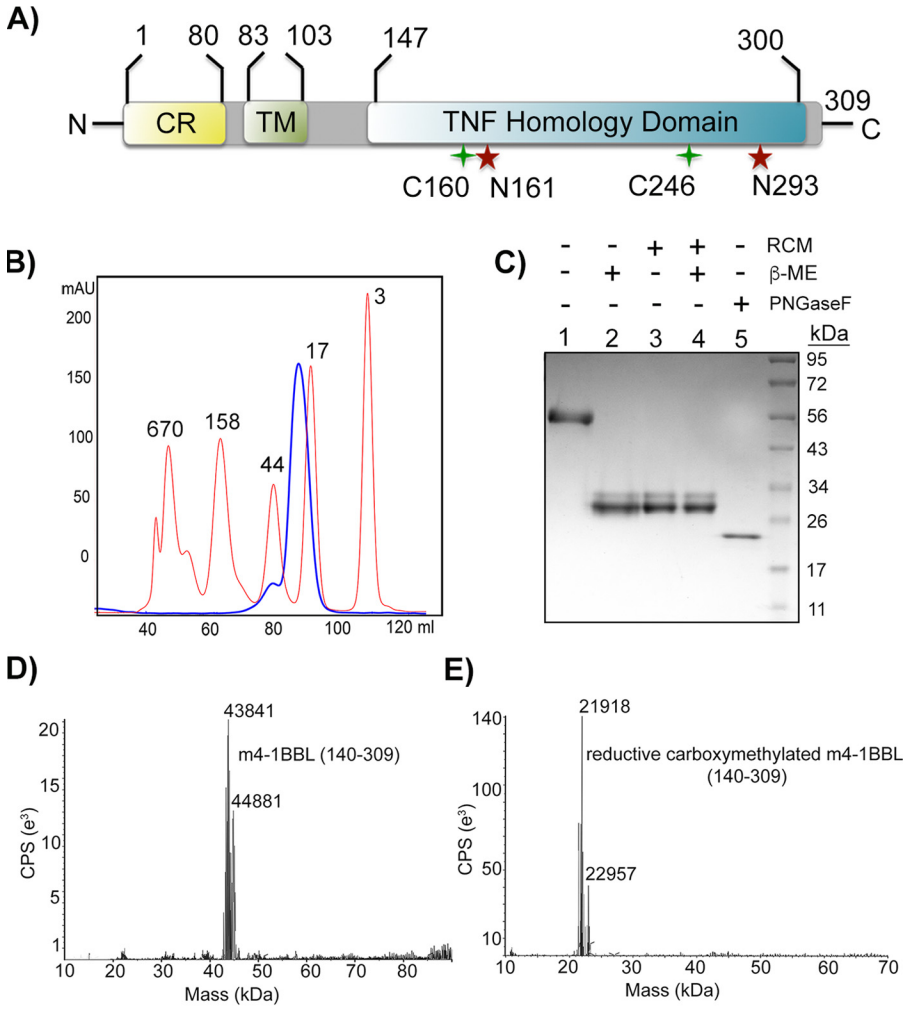

Figure 5. Expression of m4-1BBL and binding interaction with m4-1BB. *A,* schematic representation of m4-1BBL depicting the CR (cytoplasmic region), transmembrane region (*TM*), and THD. *, potential *N*-linked glycosylation sites Asn-161 and Asn-293, as well as two extra cysteines (compared with h4-1BBL) in the THD region are indicated. *B,* SEC profile of purified m4-1BBL 140–309 (*blue line*) compared with a protein standard with molecular mass in kDa (*red line*). *C,* SDS-PAGE of m4-1BBL under non-reducing (−*β-ME*) and reducing (+*β-ME*) conditions. *Lane 5* corresponds to m4-1BBL treated with PNGase F to remove *N*-glycans, which also reduces the protein. *D* and *E,* mass spectrometric analysis of m4-1BBL. *D,* ESI of wildtype m4-1BBL (140–309) determines the molecular mass of ~43.7 kDa. *E,* ESI spectra for m4-1BBL subjected to standard reduction and *S*-carboxymethylation reaction confirmed the reduction of disulfide-linked dimer to a monomer with half the molecular mass (~21.9 kDa).

m4-1BBL, corresponding to the upper band in the SDS-PAGE (Fig. 5*C*). In addition, there are some minor m4-1BBL species with similar M_r, likely representing m4-1BB species with slight heterogeneity in the size of the *N*-linked glycan. To our knowledge, this is the first report of any THD exhibiting this type of disulfide-mediated dimerization behavior. Prior studies of the human homologue revealed that, unlike m4-1BBL, h4-1BBL behaves as a trimer in gel filtration and dissociates into monomers under nonreducing conditions (13, 33).

Binding of m4-1BBL to m4-1BB

The interaction between the THD of m4-1BBL and m4-1BB was further examined by surface plasmon resonance (SPR). First, we determined the affinity of this interaction by immobilizing biotinylated m4-1BBL on the streptavidin-coated CAP sensor chip surface. We performed single cell kinetics to calculate association and dissociation of the m4-1BB–m4-1BBL complex by injecting various concentrations of monomeric m4-1BB (CRD1–4) as analyte (Fig. 6*A*, Table 2). The binding of 4-1BB to its ligand appeared both specific and saturable and analysis of reference-subtracted sensorgrams revealed that m4-1BB bound to m4-1BBL with high affinity of K_D = 8.2 nM ($k_{on} = 3 \times 10^6$ M^{-1} s^{-1} and $k_{off} = 2.5 \times 10^{-2}$ s^{-1}). In addition, we calculated the avidity contribution by measuring the binding affinity of dimeric m4-1BB-Fc to immobilized m4-1BBL. We observed a roughly 100-fold increase in binding affinity (K_D = 0.09 nM, $k_{on} = 6.6 \times 10^5$ M^{-1} s^{-1} and $k_{off} = 5.8 \times 10^{-5}$ s^{-1}) when using dimeric m4-1BB-Fc instead of 4-1BB monomers (Fig. 6*B*, Table 2). Similar binding kinetics are obtained when 4-1BB-Fc is immobilized on the sensor chip and various concentrations of m4-1BBL are passed over the receptor, again correlating with the finding that the m4-1BBL THD forms a dimer in solution (Fig. 6*C*, Table 2). The SPR data revealed that once the complex is formed, it is very stable with a k_{off} value of 1.8×10^{-4} s^{-1}. This data suggests that the interaction of dimeric m4-1BBL with two separate, monomeric m4-1BB molecules remained strong and stable due to the high avidity of this complex. It is notable that, m4-1BB bound m4-1BBL with ~10-

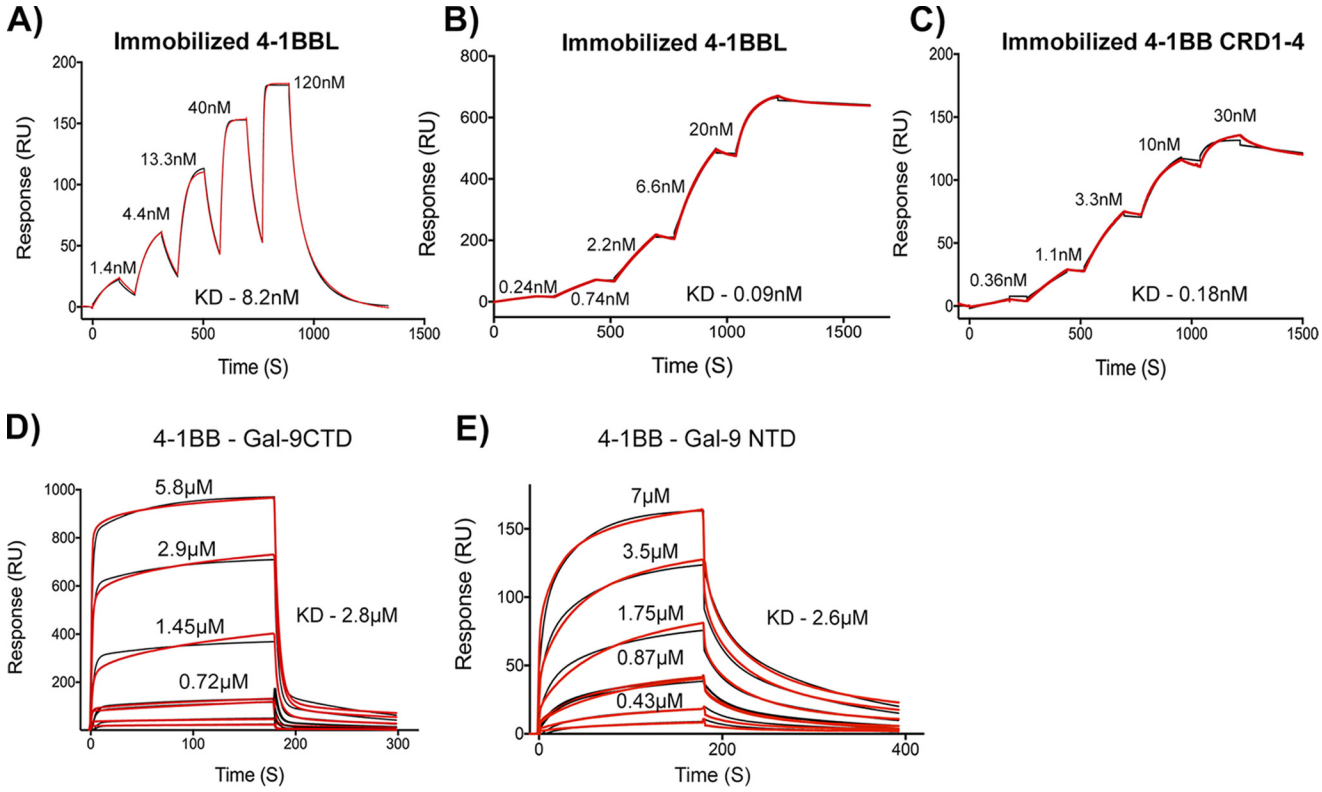

Figure 6. SPR binding analysis of m4-1BBL and Gal-9 to m4-1BB. Single cycle kinetic SPR sensorgram depicts the sequential binding response of increasing concentrations of monomeric m4-1BB (*A*) or dimeric m4-1BB-Fc (*B*) to assess avidity contribution in apparent binding affinity. *C,* single cycle kinetics to measure the interaction of dimeric m4-1BBL to immobilized m4-1BB-Fc. *D* and *E,* SPR sensorgrams for the interaction of m4-1BB (WT) with CTD (*D*) and NTD (*E*) of Gal-9. In all sensorgrams, the experimental data are shown as a *red trace* and the 1:1 fitted model as a *black solid line*.

Table 2
m4-1BB binding kinetics with Gal-9 and m4-1BBL

Immobilized (ligand)	In solution (analyte)	k_{on}	k_{off}	K_D	χ^2	K_{Deq}
		$M^{-1}\ s^{-1}$	s^{-1}	M	Response units	M
m4-1BB WT-Fc	Gal-9 NTD	3.3×10^3	8.9×10^{-3}	2.6×10^{-6}	8.87	3.2×10^{-6}
m4-1BB WT - Fc	Gal-9 CTD	1.3×10^4	3.8×10^{-2}	2.8×10^{-6}	18.4	3.8×10^{-6}
m4-1BB N128A-Fc	Gal-9 NTD	3.3×10^3	6.5×10^{-3}	1.9×10^{-6}	9.73	3.8×10^{-6}
m4-1BB N128A-Fc	Gal-9 CTD	9.1×10^3	2.1×10^{-2}	2.3×10^{-6}	11.7	3.6×10^{-6}
m4-1BB N138A-Fc	Gal-9 NTD	2.6×10^3	7.6×10^{-3}	2.9×10^{-6}	4.69	5.6×10^{-6}
m4-1BB N138A-Fc	Gal-9 CTD	5.2×10^3	2.4×10^{-2}	4.6×10^{-6}	6.99	5.4×10^{-6}
m4-1BBL	m4-1BB WT	3.0×10^6	2.5×10^{-2}	8.2×10^{-9}	3.16	10.6×10^{-9}
m4-1BBL	m4-1BB WT-Fc	6.6×10^5	5.8×10^{-5}	8.9×10^{-11}	9.7	7.0×10^{-9}
m4-1BB WT-Fc	m4-1BBL	9.8×10^5	1.8×10^{-4}	1.8×10^{-10}	3.25	2.9×10^{-9}

fold higher affinity than was reported for the human 4-1BB–h4-1BBL (K_D 2.3 nM) interaction (32, 34).

Binding of Gal-9 NTD/CTD to m4-1BB variants

We have previously demonstrated that full-length Gal-9 (containing two separate carbohydrate-binding domains) can bind to m4-1BB with high affinity to facilitate m4-1BB clustering (12). To assess the binding of the different m4-1BB constructs to Gal-9, we further generated the NTD and CTD of Gal-9 as thrombin cleavable glutathione *S*-transferase (GST) fusion proteins (Fig. S1). We assessed the real-time binding kinetics between immobilized m4-1BB-Fc and Gal-9 NTD or CTD using SPR. Unlike full-length Gal-9 that exhibited nanomolar binding toward 4-1BB (K_D = 11 nM) (12), the individual NTD and CTD domains of Gal-9 bound to m4-1BB with 1000-fold less affinity. Gal-9 CTD bound to m4-1BB-Fc with a K_D of 2.8 μM, and Gal-9 NTD bound to m4-1BB-Fc with a similar K_D of 2.5 μM (Fig. 6, *D* and *E*). However, Gal-9 CTD exhibited faster kinetics of binding to 4-1BB (Fig. 6*D*, Table 1). Because wt m4-1BB contains two *N*-linked glycans and, hence, two potential binding sites for Gal-9, the sensorgrams were fitted using the equation that corresponds to a heterogeneous ligand fit. To assess to which *N*-linked glycan galectin-9 bound, SPR experiments were performed with both *N*-linked glycan mutants of m4-1BB (N128A and N138A). This showed that both NTD and CTD of Gal-9 could bind to both *N*-glycan sites with almost similar binding affinity and SPR sensorgrams fit perfectly in a 1:1 mode of interaction with these mutants (Table 1). In summary, both *N*-linked glycans of m4-1BB (at Asn-128 and Asn-138) are able to be bound by Gal-9, presenting multiple points of attachement for Gal-9 to cluster individual m4-1BB signaling units.

Discussion

In this study, we have crystalized murine 4-1BB and characterized its interactions with murine 4-1BBL and galectin-9. We initially sought to determine the crystal structure of m4-1BB bound to each individual domain of Gal-9, but although the binding affinities were high enough to biochemically isolate the protein complexes we failed to obtain crystals of the complex. This may be due to the fact there is no intimate contact between Gal-9 and the m4-1BB protein and that Gal-9 binding to terminal galactose residues of the complex *N*-linked glycan, which itself is also not necessarily homogeneous, leads to a very flexible arrangement and prevents crystallization. Because we obtained only m4-1BB crystals, it appears that unbound m4-1BB molecules preferentially crystallized after dissociation of Gal-9, or that not all molecules were bound to each other and a minor fraction of unbound m4-1BB crystallized.

To date, the structures of TNF–TNFR complexes supported the notion that most members are similar in using the same mechanism to interact with their receptors, with a stoichiometric ratio of 3:3 to provide receptor trimerization leading to their signaling (7, 35, 36). Notable exceptions are trimeric LIGHT that primarily appears to bind 2 molecules of LTβR (37), and mouse GITRL, which in contrast to the human homotrimer only forms a homodimer (38). In addition, most of the TNF ligands except mGITRL demonstrate that two adjacent ligand protomers form a binding interface for receptor recognition surface, thereby each ligand trimer could bind to three receptor molecules. Interestingly, our studies revealed that m4-1BBL forms an unusual disulfide-linked homodimer, rather than the traditional homotrimer observed for human 4-1BBL. Hence, m4-1BBL by itself can only dimerize its receptor resulting in a 2:2 stoichiometric assembly rather a 3:3 stoichiometry as observed for human 4-1BBL–4-1BB complexes. Moreover, the positively charged residues Lys-127 and Gln-227 found in h4-1BBL (13) that form interactions with h4-1BB are replaced by negatively charged residues Glu-184 and Glu-288 in the m4-1BBL dimer. This suggests that m4-1BBL cannot form the same contacts as h4-1BBL. This divergent assembly of 4-1BBL in both species may have a profound impact in their ability to engage their receptors and hence on the overall architecture of the 4-1BB–4-1BBL complexes. The species difference observed for 4-1BBL in mouse and human is not unique. GITRL in human and mouse also exists in trimer and dimer forms and biochemical interpretations suggested a distinct mode of interaction with GITR (35, 38).

Dimerization of TNF receptors has also been observed by viral proteins. HCMV encodes dimeric UL141, which dimerizes two TRAIL-R2 monomers upon binding (39–41). Although the major function of UL141 is to retain TRAIL-R2 in the endoplasmic reticulum and down-regulate cell surface expression, UL141 does not target TRAIL-R2 for degradation by the proteasome (41). This suggests that retaining TRAIL-R2 is beneficial for the virus but whether dimerizing of TRAIL-R2 by UL141 is sufficient for signaling is currently unknown.

Many TNF receptors (*e.g.* 4-1BB, GITR, CD70, CD95, and TRAILR2) are poorly activated upon binding to their soluble ligands, but strong activation and cellular response can be achieved by either multimerization of the soluble ligands (33, 34) or their immobilization and cross-linking through binding to extracellular matrix proteins or being expressed on the surface of cells (32). In this context, galectins could also facilitate activation by enhancing the clustering of receptors, and Gal-3 has been implicated in TRAILR2 or CD95 regulation (42, 43), and our recent findings demonstrated the involvement of Gal-9 in the activation of m4-1BB as m4-1BB signaling was greatly reduced in Gal-9–deficient cells and mice (12). Previous studies with trimeric h4-1BBL found that it could not induce a functional response when soluble (34) implying, even in the presence of Gal-9, ligating 3 monomers of 4-1BB is insufficient for functional activity of 4-1BB. Furthermore, our previous studies found that a His-tagged version of soluble m4-1BBL when dimerized by anti-His was not sufficient to overcome the need for Gal-9 for activation of cells (12). However, a multimeric version of m4-1BBL that minimally contained nonamers as well as some higher order complexes could activate cells that lacked Gal-9,[3] suggesting perhaps that as many as 9 4-1BB monomers need to be clustered closely together to signal effectively. As we found m4-1BBL is a dimer, or potentially a tetramer when expressed with the stalk region, it will only engage 2 to 4 m4-1BB molecules if Gal-9 could not bridge several dimers or tetramers together and cause further oligomerization. The dimerization of two 4-1BB receptors would not favor the association of their cytoplasmic tails containing TRAF recruitment motifs with the intracellular trimeric TRAF adaptors. Gal-9 will then promote further clustering of initially formed m4-1BBL$_2$–m4-1BB$_2$ complexes, for efficient intracellular TRAF recruitment. Whether there is less dependence on Gal-9 for human 4-1BB signaling, because h4-1BBL is a homotrimer is currently unknown. However, we did show that Gal-9 binds h4-1BB similar to m4-1BB (12) and the structure of h4-1BBL suggests that the three-bladed propeller-like assembly of the homotrimer will result in the 4-1BB cytoplasmic tails to be spread far apart (open conformation), which may disfavor TRAF binding or clustering. The required distance for efficient TRAF recruitment is ~55 Å (44, 45), and we propose that in this instance Gal-9 can assist in the formation of a closed conformation by binding to two 4-1BB molecules within the same 4-1BBL–4-1BB complex as well as in different complexes. In summary, Gal-9 may enhance 4-1BB signaling using two non-mutually exclusive mechanisms. One in which Gal-9 leads to clustering of individual dimeric 4-1BB signaling units and two in which Gal-9 induces the formation of a closed state in the cytoplasmic tails of the dimers of 4-1BB that allows for efficient binding to TRAFs.

Experimental procedures

Design of m4-1BB, m4-1BB ligand, and Gal-9 constructs

The mouse (m)4-1BB ectodomain containing four CRD (1–4; amino acids 23–160) was produced in a mammalian expression system. The cDNA encoding CRD 1–4 of m4-1BB was cloned downstream of the N-terminal HA signal and upstream of the C-terminal Fc domain of human IgG1 in a

[3] M. Croft, unpublished data.

modified mammalian expression vector pCR3. A thrombin cleavage site (LVPRGS) was inserted between m4-1BB and the C-terminal Fc domain to generate m4-1BB protein for structural studies. m4-1BB ligand (m4-1BBL) was made in an insect cell expression system. m4-1BBL containing a C-terminal extracellular TNF homology domain (amino acids 140–309) was cloned downstream of the gp67 secretion signal sequence into the baculovirus transfer vector (pAcGP67A). An N-terminal His_6 tag followed by a BirA tag and thrombin cleavage site was introduced upstream of m4-1BBL to assist its purification. Galectin-9 has N-terminal and C-terminal carbohydrate-binding domains. The cDNA encoding NTD (aa 1–157) and CTD (aa 185–322) of galectin-9 were cloned separately into pGEX4T2 vector containing a N-terminal GST tag followed by a thrombin cleavage site and further purified as soluble GST-tagged proteins using a bacterial expression system.

Expression and purification of m4-1BB from mammalian HEK293T cells

The mammalian expression vector pCR3 containing the mouse 4-1BB was transiently transfected into mammalian HEK293T cells cultured in 1× Dulbecco's modified Eagle's medium (supplemented with 100 units/ml of penicillin, 100 μg/ml of streptomycin, 2 mM L-glutamine, 100 mM HEPES buffer solution and 10% (v/v) fetal bovine serum) using standard calcium phosphate transfection. After 12–16 h of transfection, the culture media was changed to fresh 1× Dulbecco's modified Eagle's medium containing 5% fetal bovine serum and the transfected 293T cells were maintained at 37 °C under 5% CO_2 for 72 h for protein expression. Supernatant containing secreted m4-1BB-Fc protein was collected and buffer exchanged against 1 × PBS (phosphate-buffered saline) by tangential flow-through filtration using 10-kDa molecular mass cut-off membranes. The supernatant was loaded on to HiTrap™ protein A HP column and m4-1BB-Fc was eluted with 100 mM sodium citrate, pH 3.0, buffer. The protein was further purified by size exclusion chromatography using a Superdex S200 column in 50 mM HEPES and 150 mM NaCl buffer and the peak fractions were concentrated and stored at −80 °C. For crystallization studies, the Fc fusion tag of m4-1BB-Fc was removed by thrombin digestion using 5 units of bovine thrombin/mg of protein at room temperature for 8 h. The cleaved m4-1BB extracellular domain was collected in the flow-through fraction of the protein A column, whereas free Fc and the uncleaved protein were removed by affinity chromatography. m4-1BB was further purified by size exclusion chromatography.

Generation of m4-1BB N-linked glycosylation site mutants

Mouse 4-1BB has two predicted *N*-linked glycans at positions Asn-128 and Asn-138. The two *N*-linked glycosylation sites of m4-1BB at positions Asn-128 and Asn-138 were exchanged against alanine by site-directed mutagenesis using the QuikChange II Multi-site Mutagenesis Kit (Stratagene, La Jolla, CA) and confirmed by sequencing. Both N128A and N138A mutants of m4-1BB were transiently transfected in HEK293T cells and the proteins were purified as described above.

Protein expression and purification of m4-1BB ligand from insect cells

The baculovirus transfer vector pAcGp67A containing the m4-1BB ligand (amino acids 140–309) construct was transfected aseptically into BacPAK6DNA according to the manufacturer's protocol. The transfection mixture was prepared by gently mixing 1 μg of transfer vector containing the target gene, 5 μl of BacPAK6DNA, 4 μl of Bacfectin reagent in a total volume to 100 μl of serum-free media without any antibiotics and further incubated at room temperature in a dark environment. As a control, the transfection mixture that lacks the BacPAK6DNA was used. Both the control and the transfection mixture were added to the seeded 2×10^6 healthy dividing *Spodoptera frugiperda* (Sf) 9 cells and grown for 5 days at 27 °C in serum-free medium containing antibiotics 100 units/ml of penicillin and 100 μg/ml of streptomycin. Two rounds of virus amplification were performed with the transfected virus (multiplicity of infection <1). For protein production, several individual 2-liter Erlenmeyer flasks seeded with 2×10^6 Sf9 cells/ml were infected with high titer recombinant virus stock (made from low titer virus multiplicity of infection = 1 of second virus amplification) and grown as suspension culture (135 rpm) at 27 °C. After 72–84 h of growth, the cell supernatant was collected by centrifugation and then buffer exchanged against 1× PBS using a Millipore filtration device and a 10-kDa molecular mass cut-off membrane. The supernatant was loaded on to nickel-nitrilotriacetic acid column and washed with 20 mM imidazole. The His-tagged m4-1BB ligand was eluted with 250 mM imidazole and later the tag was removed by thrombin cleavage at room temperature. The m4-1BB ligand was further purified by size exclusion chromatography using Superdex 200 column. The protein was concentrated to 10 mg/ml and used for biochemical studies.

Reductive carboxymethylation (RCM) of m4-1BB ligand

For RCM, 1 mg of m4-1BBL was reconstituted in 1 ml of 10 mM Tris, pH 8.5, and then reduced for 1 h at 37 °C in the presence of 10 mM DTT followed by cooling the sample to ambient temperature. Next, the reduced sample was incubated with 25 mM iodoacetic acid for 30 min in the dark at room temperature to ensure the exchange of free cysteine to *S*-carboxymethylated cysteine. The reaction of iodoacetic acid was quenched by adding 20 mM DTT and the RCM-treated m4-1BBL was further buffer exchanged against 50 mM HEPES and 150 mM NaCl using a spin column.

Expression and protein purification of human and mouse Gal-9 constructs

The expression and purification of human and mouse galectin-9 NTD and CTD have been reported earlier (12, 46, 47). Briefly, the N-terminal and C-terminal domains of human and mouse galectin-9 were expressed as GST-tagged proteins in *Escherichia coli* BL21 DE3 cells, grown in LB medium, and induced by the addition of 0.4 mM isopropyl 1-thio-β-D-galactopyranoside at 16 °C for 16 h. The cells were disrupted by sonication in lysis buffer (10 mM Tris, pH 7.5, 500 mM NaCl, 1 mM EDTA, 5 mM β-mercaptoethanol, and 1 mM phenylmethylsulfonyl fluoride). The supernatants were treated with 1% Tri-

ton X-100, stirred at 4 °C for 1 h before loading onto glutathione-Sepharose 4B GST affinity columns (GSTrap 4B), and the GST fusion proteins were eluted in 20 mM glutathione and 50 mM NaCl buffer. The NTD and CTD of galectin-9 were separated from the GST fusion tag by thrombin cleavage at room temperature for 6 h using 5 units of bovine thrombin/mg of protein. After thrombin digestion, the untagged NTD and CTD of galectin-9 were further purified by size exclusion chromatography using Superdex S-75 and pure fractions were concentrated and stored at −80 °C. The purity of the proteins was confirmed by SDS-polyacrylamide gel electrophoresis.

Crystallization of m4-1BB

Purified m4-1BB and slight excess of either the N- or C-terminal domains of Gal-9 were mixed separately and both complexes were isolated using a Superdex S-200 size exclusion column in 50 mM HEPES and 150 mM NaCl, pH 7.5, running buffer (Fig. S1). Both m4-1BB–Gal-9 complexes were concentrated to 3.5 mg/ml and subjected to crystallization. Initial crystallization trials were performed in a 96-well format using a nanoliter dispensing liquid handling robot (Art Robbins Phenix) and mixing equal amounts of protein and precipitant from different commercially available crystallization screens (JCSG core+, 1–4, Wizard, MB suite and PEG ion screens). Over 800 crystallization conditions were tested using the sitting drop vapor diffusion method. Optimization of all crystallization conditions was performed manually by both hanging drop and sitting drop methods. Crystals were obtained in various conditions, however, only two conditions yielded high quality diffraction crystals and all analyzed crystals only contained m4-1BB. Of these conditions, one crystal (space group P21) was grown over 4 days at 22 °C using the precipitant 0.1 M sodium acetate, pH 4.5, 30% (w/v) polyethylene glycol (PEG) 8000, and 0.2 M lithium sulfate. The second crystal belongs to space group $P2_12_12$ and was grown at room temperature over 10 days using a high pH buffer containing 0.1 M Bicine and 30% (w/v) PEG 6000. Crystals containing the m4-1BB N128A mutant were grown in 50 mM HEPES and 150 mM NaCl, pH 7.5, and 1 0.1 M sodium acetate, pH 4.5, 30% (w/v) PEG 8000, 0.2 M lithium sulfate, respectively. All crystals were flash-cooled in liquid nitrogen in their crystallization buffer containing 20% glycerol for subsequent data collection.

Data collection and refinement

Native diffraction data for different crystal forms was collected remotely at Stanford Synchrotron Radiation Light Source (SSRL) beam line 9-2 using a PILATUS 6M PAD detector at a wavelength of 0.97 Å and a temperature of 100 K. Each image was collected at 0.25 degrees oscillation and a 5-s exposure time. The data were processed and scaled using HKL2000 (48). Phasing using the molecular replacement method (PHASER-MR (49)) and the known structures of TNFRs that share ~30% sequence identity with m4-1BB as a starting model was unsuccessful. Therefore, we have experimentally determined the phase information by sulfur-SAD phasing by collecting diffracting data on several crystals that belong to $P2_12_12$ space group enhancing the sulfur anomalous signal at 2.07 Å.

Sulfur (S)-SAD phasing method

Special care was taken to collect with the best exposure to extract good quality diffraction without unnecessary damaging the crystal. Measuring a small anomalous signal needed a lot of redundancy and relatively strong I/σ, both of which were achieved by collecting 1080 degrees for one crystal and 720 degrees for another crystal. The ISa values for the individual datasets were between 27.0 and 34.9 indicating proper exposure and high crystal diffraction quality. The beam size was adjusted to 80 by 80 μm to match the crystal size and decrease the diffraction image background. The calculated flux at the sample position under these conditions was 2.3×10^9 photons/s and each image was collected for 5 s for 0.5 degree oscillation, in inverse beam geometry with a wedge of 10 degrees.

Diffraction data processing

The collected images were processed with XDS (50), as implemented in the AUTOXDS script at SSRL (Ana Gonzalez). Multiple datasets were scaled together in its scaling program XSCALE with the option to keep anomalous reflections separate (51). The overall resolution was 2.5 Å (CC1/2 = 59%, I/σ = 1.50), with a significant anomalous signal (>15%) extending to 2.97-Å resolution. Overall I/σ was 33.0 and the anomalous correlation was 44%. On average the reflections were observed ~70-fold. XDSCONV was used to convert to mtz format used in the refinement. The space group was $P2_12_12$ (sg 18), with unit cell dimensions: $a = 65.05$ Å, $b = 67.76$ Å, $c = 87.99$ Å, $\alpha = \beta = \gamma = 90°$.

Phasing

The XSCALE output was forwarded into the HKL2MAP (version 0.3.i-β), which is a graphical interface for the SHELXCDE programs (52). SHELXC also evaluated the anomalous signal to be significant to 3.0 Å. Within SHELXD the search for 20 sulfur sites in the 40–3.5-Å range was successful (16 solutions in 10,000 tries) only after adding the 5th 360-degree dataset, but not before, confirming the need for higher accuracy and signal strength based on higher redundancy of observations of slow decaying diffraction crystals. Characteristic bimodal distribution was observed in the CCall/CCweak and CCall/CFOM graphs. The highest peak had the following values CFOM = 66.7, CCall = 49.1 and CCweak = 17.6. The decrease in resolution from 3.0 to 3.5 Å for the sites search was required to increase the strength of the signal. Within SHELXE, the solvent fraction of 61% was applied based on the expected cell content. The option to do a secondary structure search and placement was also activated. The inverse phase had better phases and resulted in interpretable electron density maps with the sulfur positions coinciding with good density between the secondary structure elements. Due to lower resolution only a single sulfur position was found per each pair of disulfides. Only 8 cycles of density improvement were enough to show significant contrast and connectivity with an estimated CC map over 0.8. 171 peptides (amino acids) were autobuilt into the density with a protein-like architecture. The overall CC (trace, native) for the inverted phases was 30.42% well over the critical 25% indicating a clear solution. The original phases had only ~12% CC (trace, native).

Model building

The model and improved phases from SHELXE were used in BUCCANEER (53) as part of the CCP4 suite (54) to complete the model building. Manual fixes and improvements in the model were performed in COOT (55, 56).

Refinement

The final model was refined in PHENIX/REFMAC (57) to 2.5-Å resolution with residual factors $R/R_{free} = 21.3/27.9\%$. The model had excellent stereochemistry with only 2 residues as Ramachandran outliers, which are confirmed by the electron density. Using the above structure as a search model in Phaser MR (49), we have refined the structures of both m4-1BB CRD 1–4 that belongs to the $P2_1$ space group and m4-1BB CRD 1–4 N128A mutant by molecular replacement in Phenix refine and Refmac5 (58, 59). The model building was performed in COOT with good Ramachandran statistics of 99% residues in allowed region.

SPR binding kinetics

All the binding studies were performed on a BIACORE T200 instrument at 293 K. HBS-EP (10 mM HEPES, 150 mM NaCl, 3 mM EDTA, and 0.05% surfactant Tween 20) was used as running buffer for immobilization and kinetic binding analysis and all the proteins were diluted in this buffer prior to the experiment. Kinetic characterization of mouse Gal-9 NTD and CTD binding to wildtype and variants of m4-1BB-Fc was done using m4-1BB-Fc variants as ligands and Gal-9 constructs as analytes. For kinetic experiments, the SPR surfaces were prepared by immobilizing anti-human IgG (Fc) antibody on a CM5 sensor chip (GE Healthcare) by amine coupling using standard EDC-NHS chemistry followed by ethanolamine blocking. m4-1BB-Fc, and both N128A and N138A mutants at concentrations of 20 μg/ml were captured on the sensor chip at 200–400 response units. A reference surface containing only free Fc was used for background subtraction. Kinetic experiments were performed by injecting various increasing concentrations of analytes at a flow rate of 30 μl/min over immobilized proteins in both active and reference channels for 180–240-s association, and dissociation was monitored for an additional 600 s at a flow rate of 30 μl/min. The biosensor surface regeneration was carried out by injecting 3 M $MgCl_2$ for 30 s at a flow rate of 20 μl/min followed by running buffer at 60 μl/min. One middle concentration of each analyte was injected in duplicate in at least two separate experiments. The interaction of Gal-9 constructs with immobilized m4-1BB variants was monitored in real time and expressed with a sensorgram reporting magnitude of response in relative units.

For binding studies of m4-1BB and m4-1BBL, first, biotinylated m4-1BBL was captured on the CAP chip surface using a biotin capture kit according to the manufacturer's instructions to achieve the immobilization level of ~500 response units. A control surface with saturated amounts of biotin was also prepared. For single-cell kinetic analysis, increasing concentrations of both Fc-tagged and Fc tag removed m4-1BB (CRD1–4) in two separate experiments were injected on both the immobilized and control surfaces at a flow rate of 30 μl/min for 120 s association followed by a dissociation of 100 s between each cycle. The final dissociation was performed by flowing running buffer at a flow rate of 30 μl/min for 1000 s. The cycle ended with fully regeneration of the surface with a mixture (3:1, v/v) of 8 M guanidine HCl and 1 M NaOH followed by stabilization period of 60 s. For reverse kinetics, Fc-tagged m4-1BB was immobilized on anti-Fc-coated CM5 surface (active surface) and free Fc-immobilized surface used as reference. Later, increasing concentrations of m4-1BBL as analyte was injected on both surfaces for 120 s and its dissociation for each cycle was recorded for 100 s (flow rate of 30 μl/min) with a final dissociation of 1000 s.

All binding curves were corrected for background and bulk refractive index contribution by subtraction of the reference flow cells response from active surface. Models were fitted globally across the data sets for each concentration of analyte. Obtained kinetic data were analyzed using the Biacore T200 Evaluation software 2.0 (GE Healthcare) under a theoretical 1:1 Langmuir interaction kinetic model describing 1:1 binding between analyte (A) and ligand (B) to calculate the association rate (k_a) and the dissociation rate (k_d) and the equilibrium dissociation constant ($K_D = k_d/k_a$) by non-linear fitting.

Author contributions—A. B. conducted most of the biochemical and structural experiments, analyzed the results, and drafted the paper. T. D. collected anomalous data and solved the structure by S-SAD phasing. J. W. assisted with biochemical experiments. G. P. assisted in m4-1BB expression in HEK293T cells. C. A. B. supervised G. P. and edited the manuscript. M. C. conceived the overall project with D. M. Z. and edited the paper. D. M. Z. conceived the experiments, supervised the overall project and wrote the manuscript.

Acknowledgments—We thank the Stanford Synchrotron Lightsource (SSRL) for access to remote data collection and the SSRL beamline scientists for support. Use of the Stanford Synchrotron Radiation Lightsource, SLAC National Accelerator Laboratory, is supported by the United States Dept. of Energy, Office of Science, Office of Basic Energy Sciences under Contract DE-AC02–76SF00515. The SSRL Structural Molecular Biology Program is supported by the DOE Office of Biological and Environmental Research, and by National Institutes of Health, NIGMS Grant P41GM103393.

References

1. Croft, M., Benedict, C. A., and Ware, C. F. (2013) Clinical targeting of the TNF and TNFR superfamilies. *Nat. Rev. Drug Discov.* **12,** 147–168 CrossRef Medline
2. Watts, T. H. (2005) TNF/TNFR family members in costimulation of T cell responses. *Annu. Rev. Immunol.* **23,** 23–68 CrossRef Medline
3. Aggarwal, B. B. (2003) Signalling pathways of the TNF superfamily: a double-edged sword. *Nat. Rev. Immunol.* **3,** 745–756 CrossRef Medline
4. Chattopadhyay, K., Lazar-Molnar, E., Yan, Q., Rubinstein, R., Zhan, C., Vigdorovich, V., Ramagopal, U. A., Bonanno, J., Nathenson, S. G., and Almo, S. C. (2009) Sequence, structure, function, immunity: structural genomics of costimulation. *Immunol. Rev.* **229,** 356–386 CrossRef Medline
5. Croft, M. (2003) Co-stimulatory members of the TNFR family: keys to effective T-cell immunity? *Nat. Rev. Immunol.* **3,** 609–620 CrossRef Medline
6. Croft, M. (2009) The role of TNF superfamily members in T-cell function and diseases. *Nat. Rev. Immunol.* **9,** 271–285 CrossRef Medline
7. An, H.-J., Kim, Y. J., Song, D. H., Park, B. S., Kim, H. M., Lee, J. D., Paik, S.-G., Lee, J.-O., and Lee, H. (2011) Crystallographic and mutational anal-

ysis of the CD40-CD154 complex and its implications for receptor activation. *J. Biol. Chem.* **286,** 11226–11235 CrossRef
8. Mukai, Y., Nakamura, T., Yoshikawa, M., Yoshioka, Y., Tsunoda, S., Nakagawa, S., Yamagata, Y., and Tsutsumi, Y. (2010) Solution of the structure of the TNF-TNFR2 complex. *Sci. Signal.* **3,** ra83 Medline
9. Banner, D. W., D'Arcy, A., Janes, W., Gentz, R., Schoenfeld, H.-J., Broger, C., Loetscher, H., and Lesslauer, W. (1993) Crystal structure of the soluble human 55 kd TNF receptor-human TNFβ complex: implications for TNF receptor activation. *Cell* **73,** 431–445 CrossRef Medline
10. Lee, S.-W., and Croft, M. (2009) 4-1BB as a therapeutic target for human disease. in *Therapeutic Targets of the TNF Superfamily* (Grewal, I. S., ed) pp. 120–129, Springer New York
11. Kwon, B. S., and Weissman, S. M. (1989) cDNA sequences of two inducible T-cell genes. *Proc. Natl. Acad. Sci. U.S.A.* **86,** 1963–1967 CrossRef Medline
12. Madireddi, S., Eun, S.-Y., Lee, S.-W., Nemčovičová, I., Mehta, A. K., Zajonc, D. M., Nishi, N., Niki, T., Hirashima, M., and Croft, M. (2014) Galectin-9 controls the therapeutic activity of 4-1BB–targeting antibodies. *J. Exp. Med.* **211,** 1433–1448 CrossRef Medline
13. Won, E.-Y., Cha, K., Byun, J.-S., Kim, D.-U., Shin, S., Ahn, B., Kim, Y. H., Rice, A. J., Walz, T., Kwon, B. S., and Cho, H.-S. (2010) The structure of the trimer of human 4-1BB ligand is unique among members of the tumor necrosis factor superfamily. *J. Biol. Chem.* **285,** 9202–9210 CrossRef
14. Bodmer, J. L., Schneider, P., and Tschopp, J. (2002) The molecular architecture of the TNF superfamily. *Trends Biochem. Sci.* **27,** 19–26 CrossRef Medline
15. Pollok, K. E., Kim, Y.-J., Hurtado, J., Zhou, Z., Kim, K. K., and Kwon, B. S. (1994) 4-1BB T-cell antigen binds to mature B cells and macrophages, and costimulates anti-μ-primed splenic B cells. *Eur. J. Immunol.* **24,** 367–374 CrossRef Medline
16. Snell, L. M., Lin, G. H., McPherson, A. J., Moraes, T. J., and Watts, T. H. (2011) T-cell intrinsic effects of GITR and 4-1BB during viral infection and cancer immunotherapy. *Immunol. Rev.* **244,** 197–217 CrossRef Medline
17. Jang, I. K., Lee, Z. H., Kim, Y. J., Kim, S. H., and Kwon, B. S. (1998) Human 4-1BB (CD137) Signals are mediated by TRAF2 and activate nuclear factor-κB. *Biochem. Biophys. Res. Commun.* **242,** 613–620 CrossRef Medline
18. Arch, R. H., and Thompson, C. B. (1998) 4-1BB and Ox40 are members of a tumor necrosis factor (TNF)-nerve growth factor receptor subfamily that bind TNF receptor-associated factors and activate nuclear factor κB. *Mol. Cell. Biol.* **18,** 558–565 CrossRef Medline
19. Stärck, L., Scholz, C., Dörken, B., and Daniel, P. T. (2005) Costimulation by CD137/4-1BB inhibits T cell apoptosis and induces Bcl-xL and c-FLIP-short via phosphatidylinositol 3-kinase and AKT/protein kinase B. *Eur. J. Immunol.* **35,** 1257–1266 CrossRef Medline
20. Bansal-Pakala, P., and Croft, M. (2002) Defective T cell priming associated with aging can be rescued by signaling through 4-1BB (CD137). *J. Immunol.* **169,** 5005–5009 CrossRef Medline
21. Halstead, E. S., Mueller, Y. M., Altman, J. D., and Katsikis, P. D. (2002) *In vivo* stimulation of CD137 broadens primary antiviral CD8+ T cell responses. *Nat. Immunol.* **3,** 536–541 CrossRef Medline
22. Wada, J., and Kanwar, Y. S. (1997) Identification and characterization of galectin-9, a novel β-galactoside-binding mammalian lectin. *J. Biol. Chem.* **272,** 6078–6086 CrossRef Medline
23. Wada, J., Ota, K., Kumar, A., Wallner, E. I., and Kanwar, Y. S. (1997) Developmental regulation, expression, and apoptotic potential of galectin-9, a β-galactoside binding lectin. *J. Clin. Investig.* **99,** 2452–2461 CrossRef Medline
24. Liu, F. T., and Rabinovich, G. A. (2005) Galectins as modulators of tumour progression. *Nat. Rev.* **5,** 29–41
25. Rabinovich, G. A., Liu, F. T., Hirashima, M., and Anderson, A. (2007) An emerging role for galectins in tuning the immune response: lessons from experimental models of inflammatory disease, autoimmunity and cancer. *Scand. J. Immunol.* **66,** 143–158 CrossRef Medline
26. Ru, H., Zhao, L., Ding, W., Jiao, L., Shaw, N., Liang, W., Zhang, L., Hung, L.-W., Matsugaki, N., Wakatsuki, S., and Liu, Z.-J. (2012) S-SAD phasing study of death receptor 6 and its solution conformation revealed by SAXS. *Acta Crystallogr. D Biol. Crystallogr.* **68,** 521–530 CrossRef
27. Nelson, C. A., Warren, J. T., Wang, M. W., Teitelbaum, S. L., and Fremont, D. H. (2012) RANKL employs distinct binding modes to engage RANK and the osteoprotegerin decoy receptor. *Structure* **20,** 1971–1982 CrossRef Medline
28. Zhou, Z., Tone, Y., Song, X., Furuuchi, K., Lear, J. D., Waldmann, H., Tone, M., Greene, M. I., and Murali, R. (2008) Structural basis for ligand-mediated mouse GITR activation. *Proc. Natl. Acad. Sci. U.S.A.* **105,** 641–645 CrossRef
29. Naismith, J. H., and Sprang, S. R. (1998) Modularity in the TNF-receptor family. *Trends Biochem. Sci.* **23,** 74–79 CrossRef Medline
30. Magis, C., van der Sloot, A. M., Serrano, L., and Notredame, C. (2012) An improved understanding of TNFL/TNFR interactions using structure-based classifications. *Trends Biochem. Sci.* **37,** 353–363 CrossRef Medline
31. Loo, D. T., Chalupny, N. J., Bajorath, J., Shuford, W. W., Mittler, R. S., and Aruffo, A. (1997) Analysis of 4-1BBL and laminin binding to murine 4-1BB, a member of the tumor necrosis factor receptor superfamily, and comparison with human 4-1BB. *J. Biol. Chem.* **272,** 6448–6456 CrossRef
32. Lang, I., Füllsack, S., Wyzgol, A., Fick, A., Trebing, J., Arana, J. A. C., Schäfer, V., Weisenberger, D., and Wajant, H. (2016) Binding studies of TNF receptor superfamily (TNFRSF) receptors on intact cells. *J. Biol. Chem.* **291,** 5022–5037 CrossRef
33. Wyzgol, A., Müller, N., Fick, A., Munkel, S., Grigoleit, G. U., Pfizenmaier, K., and Wajant, H. (2009) Trimer stabilization, oligomerization, and antibody-mediated cell surface immobilization improve the activity of soluble trimers of CD27L, CD40L, 41BBL, and glucocorticoid-induced TNF receptor ligand. *J. Immunol.* **183,** 1851–1861 CrossRef Medline
34. Rabu, C., Quéméner, A., Jacques, Y., Echasserieau, K., Vusio, P., and Lang, F. (2005) Production of recombinant human trimeric CD137L (4-1BBL): cross-linking is essential to its t cell co-stimulation activity. *J. Biol. Chem.* **280,** 41472–41481 CrossRef
35. Chattopadhyay, K., Ramagopal, U. A., Mukhopadhaya, A., Malashkevich, V. N., DiLorenzo, T. P., Brenowitz, M., Nathenson, S. G., and Almo, S. C. (2007) Assembly and structural properties of glucocorticoid-induced TNF receptor ligand: implications for function. *Proc. Natl. Acad. Sci. U.S.A.* **104,** 19452–19457 CrossRef
36. Compaan, D. M., and Hymowitz, S. G. (2006) The crystal structure of the costimulatory OX40-OX40L complex. *Structure* **14,** 1321–1330 CrossRef Medline
37. Eldredge, J., Berkowitz, S., Corin, A. F., Day, E. S., Hayes, D., Meier, W., Strauch, K., Zafari, M., Tadi, M., and Farrington, G. K. (2006) Stoichiometry of LTβR binding to LIGHT. *Biochemistry* **45,** 10117–10128 CrossRef Medline
38. Chattopadhyay, K., Ramagopal, U. A., Brenowitz, M., Nathenson, S. G., and Almo, S. C. (2008) Evolution of GITRL immune function: murine GITRL exhibits unique structural and biochemical properties within the TNF superfamily. *Proc. Natl. Acad. Sci. U.S.A.* **105,** 635–640 CrossRef
39. Nemčovičová, I., Benedict, C. A., and Zajonc, D. M. (2013) Structure of human cytomegalovirus UL141 binding to TRAIL-R2 reveals novel, non-canonical death receptor interactions. *PLoS Pathog.* **9,** e1003224 CrossRef Medline
40. Nemčovičová, I., and Zajonc, D. M. (2014) The structure of cytomegalovirus immune modulator UL141 highlights structural Ig-fold versatility for receptor binding. *Acta Crystallogr. D Biol. Crystallogr.* **70,** 851–862 CrossRef Medline
41. Smith, W., Tomasec, P., Aicheler, R., Loewendorf, A., Nemčovičová, I., Wang, E. C., Stanton, R. J., Macauley, M., Norris, P., Willen, L., Ruckova, E., Nomoto, A., Schneider, P., Hahn, G., Zajonc, D. M., *et al.* (2013) Human cytomegalovirus glycoprotein UL141 targets the TRAIL death receptors to thwart host innate antiviral defenses. *Cell Host Microbe* **13,** 324–335 CrossRef Medline
42. Mazurek, N., Byrd, J. C., Sun, Y., Hafley, M., Ramirez, K., Burks, J., and Bresalier, R. S. (2012) Cell-surface galectin-3 confers resistance to TRAIL by impeding trafficking of death receptors in metastatic colon adenocarcinoma cells. *Cell Death Differ.* **19,** 523–533 CrossRef Medline
43. Fukumori, T., Takenaka, Y., Oka, N., Yoshii, T., Hogan, V., Inohara, H., Kanayama, H.-o., Kim, H.-R., and Raz, A. (2004) Endogenous galectin-3

determines the routing of CD95 apoptotic signaling pathways. *Cancer Res.* **64,** 3376 CrossRef Medline
44. Ye, H., Park, Y. C., Kreishman, M., Kieff, E., and Wu, H. (1999) The structural basis for the recognition of diverse receptor sequences by TRAF2. *Mol. Cell* **4,** 321–330 CrossRef Medline
45. Park, Y. C., Ye, H., Hsia, C., Segal, D., Rich, R. L., Liou, H.-C., Myszka, D. G., and Wu, H. (2000) A novel mechanism of TRAF signaling revealed by structural and functional analyses of the TRADD–TRAF2 interaction. *Cell* **101,** 777–787 CrossRef Medline
46. Nagae, M., Nishi, N., Murata, T., Usui, T., Nakamura, T., Wakatsuki, S., and Kato, R. (2006) Crystal structure of the galectin-9 N-terminal carbohydrate recognition domain from *Mus musculus* reveals the basic mechanism of carbohydrate recognition. *J. Biol. Chem.* **281,** 35884–35893 CrossRef
47. Yoshida, H., Teraoka, M., Nishi, N., Nakakita, S.-i., Nakamura, T., Hirashima, M., and Kamitori, S. (2010) X-ray structures of human galectin-9 C-terminal domain in complexes with a biantennary oligosaccharide and sialyllactose. *J. Biol. Chem.* **285,** 36969–36976 CrossRef
48. Otwinowski, Z., and Minor, W. (1997) Processing of x-ray diffraction data collected in oscillation mode. *Methods Enzymol.* **276,** 307–326 CrossRef
49. McCoy, A. J., Grosse-Kunstleve, R. W., Storoni, L. C., and Read, R. J. (2005) Likelihood-enhanced fast translation functions. *Acta Crystallogr. D Biol. Crystallogr.* **61,** 458–464 CrossRef Medline
50. Kabsch, W. (2010) XDS. *Acta Crystallogr. D Biol Crystallogr.* **66,** 125–132 CrossRef Medline
51. Kabsch, W. (2010) Integration, scaling, space-group assignment and post-refinement. *Acta Crystallogr. D Biol. Crystallogr.* **66,** 133–144 CrossRef Medline
52. Sheldrick, G. M. (2008) A short history of SHELX. *Acta Crystallogr. A* **64,** 112–122 CrossRef Medline
53. Cowtan, K. (2006) The Buccaneer software for automated model building: 1. tracing protein chains. *Acta Crystallogr. D Biol. Crystallogr.* **62,** 1002–1011 CrossRef Medline
54. Winn, M. D., Ballard, C. C., Cowtan, K. D., Dodson, E. J., Emsley, P., Evans, P. R., Keegan, R. M., Krissinel, E. B., Leslie, A. G., McCoy, A., McNicholas, S. J., Murshudov, G. N., Pannu, N. S., Potterton, E. A., Powell, H. R., *et al.* (2011) Overview of the CCP4 suite and current developments. *Acta Crystallogr. D Biol. Crystallogr.* **67,** 235–242 CrossRef Medline
55. Emsley, P., and Cowtan, K. (2004) Coot: model-building tools for molecular graphics. *Acta Crystallogr. D Biol. Crystallogr.* **60,** 2126–2132 CrossRef Medline
56. Emsley, P., Lohkamp, B., Scott, W. G., and Cowtan, K. (2010) Features and development of Coot. *Acta Crystallogr. D Biol. Crystallogr.* **66,** 486–501 CrossRef Medline
57. Murshudov, G. N., Vagin, A. A., and Dodson, E. J. (1997) Refinement of macromolecular structures by the maximum likelihood method. *Acta Crystallogr. D Biol. Crystallogr.* **53,** 240–255 CrossRef Medline
58. Rossmann, M. G. (1972) *The Molecular Replacement Method*, Gordon & Breach, New York
59. Vagin, A. A., and Teplyakov, A. (1997) MOLREP:an automated programm for molecular replacement. *J. Appl. Cryst.* **30,** 1022–1025 CrossRef